Mon. Not. R. Astron. Soc. **000**, 000–000 (0000) Printed 29 May 2015 (MN LATEX style file v2.2)

# Galaxy shapes and alignments in the MassiveBlack-II hydrodynamic and dark matter-only simulations

Ananth Tenneti[1]*, Rachel Mandelbaum[1]†, Tiziana Di Matteo[1]‡,
Alina Kiessling[2], Nishikanta Khandai[3]
[1] *McWilliams Center for Cosmology, Department of Physics, Carnegie Mellon University, Pittsburgh, PA 15213, USA*
[2] *Jet Propulsion Laboratory, California Institute of Technology, Pasadena, CA 91109, USA*
[3] *School of Physical Sciences, National Institute of Science Education and Research, Bhubaneswar, Odisha 751005, India*

29 May 2015

arXiv:1505.03124v2 [astro-ph.CO] 28 May 2015

**ABSTRACT**

We compare the shapes and intrinsic alignments of galaxies in the MassiveBlack-II cosmological hydrodynamic simulation (MBII) to those in a dark matter-only (DMO) simulation performed with the same volume $(100h^{-1}\mathrm{Mpc})^3$, cosmological parameters, and initial conditions. Understanding the impact of baryonic physics on galaxy shapes and alignments and their relation to the dark matter distribution should prove useful to map the intrinsic alignments of galaxies from hydrodynamic to dark matter-only simulations. We find that dark matter subhalos are typically rounder in MBII, and the shapes of stellar matter in low mass galaxies are more misaligned with the shapes of the dark matter of the corresponding subhalos in the DMO simulation. At $z = 0.06$, the fractional difference in the mean misalignment angle between MBII and DMO simulations varies from $\sim 28\% - 12\%$ in the mass range $10^{10.8} - 6.0 \times 10^{14} h^{-1} M_\odot$. We study the dark matter halo shapes and alignments as a function of radius, and find that while galaxies in MBII are more aligned with the inner parts of their dark matter subhalos, there is no radial trend in their alignments with the corresponding subhalo in the DMO simulation. This result highlights the importance of baryonic physics in determining the alignment of the galaxy with respect to the inner parts of the halo. Finally, we compare the ellipticity-direction (ED) correlation for galaxies to that for dark matter halos, finding that it is suppressed on all scales by stellar-dark matter misalignment. In the projected shape-density correlation ($w_{\delta+}$), which includes ellipticity weighting, this effect is partially canceled by the higher mean ellipticities of the stellar component, but differences of order $30 - 40\%$ remain on scales $> 1$ Mpc over a range of subhalo masses, with scale-dependent effects below 1 Mpc.

**Key words:** cosmology: theory – methods: numerical – hydrodynamics – gravitational lensing: weak – galaxies: star formation

## 1 INTRODUCTION

Weak gravitational lensing is a cosmological probe that has the potential to address major outstanding cosmological problems, such as understanding the connection between dark matter and galaxies, the nature of dark energy, and exploring possible variations in the theory of gravity on cosmological scales (Albrecht et al. 2006; Weinberg et al. 2013). Using weak lensing, upcoming surveys such as the Large Synoptic Survey Telescope[1] (LSST; LSST Science Collaboration et al. 2009), Euclid[2] (Laureijs et al. 2011), and the Wide-Field Infrared Survey Telescope[3] (WFIRST; Spergel et al. 2015) will to constrain cosmological parameters such as the dark energy equation of state to a very high precision. However, the most basic weak lensing analysis assumes that galaxy shapes are randomly aligned, which is not correct in reality. The galaxy shapes are correlated with each other and with the underlying density field. This intrinsic alignment of galaxy shapes is an important astrophysical systematic that contaminates measurements in weak lensing surveys (Heavens, Refregier & Heymans 2000; Croft &

* vat@andrew.cmu.edu
† rmandelb@andrew.cmu.edu
‡ tiziana@phys.cmu.edu
[1] http://www.lsst.org/lsst/
[2] http://sci.esa.int/euclid/, http://www.euclid-ec.org
[3] http://wfirst.gsfc.nasa.gov

© 0000 RAS

Metzler 2000; Catelan, Kamionkowski & Blandford 2001; Jing 2002; Hirata & Seljak 2004). For reviews on intrinsic alignments and its impact on cosmological parameter constraints, see Troxel & Ishak (2014), Joachimi et al. (2015), Kirk et al. (2015), and Kiessling et al. (2015).

Previous studies of intrinsic alignments that made predictions out to tens of Mpc scales have generally involved analytical methods, or $N$-body and hydrodynamic simulations of cosmological volume. Analytical modeling involves a number of different possible models, with the one receiving the most attention for elliptical galaxies being the linear alignment model (Catelan, Kamionkowski & Blandford 2001; Hirata & Seljak 2004), an extension of it to nonlinear scales using the non-linear power spectrum (Bridle & King 2007; see Blazek, Vlah & Seljak 2015 for a more recent extension that includes all non-linear terms at the same order), and a small-scale extension using the halo model (Schneider & Bridle 2010). $N$-body simulations have been used to study intrinsic alignments by Heymans et al. (2006) where halos are populated with galaxies which are stochastically misaligned, Joachimi et al. (2013) with semi-analytic models, and others (see references in the review by Kiessling et al. 2015). However, the physics of galaxy formation is not taken into consideration by these analytic models and $N$-body simulations. Recent hydrodynamic simulations of cosmological volumes such as the MassiveBlack-II (Khandai et al. 2014), the Horizon-AGN (Dubois et al. 2014), and the EAGLE and cosmo-OWLS (Velliscig et al. 2015) simulations have made it possible to directly study the intrinsic alignments of the stellar component of galaxies and their scaling with mass, luminosity and distance.

Using the MassiveBlack-II (MBII) simulation, we previously studied the shapes of the stellar matter component of the galaxies and its alignment with the shape of the dark matter component (Tenneti et al. 2014). We found that the ellipticities of the stellar components of galaxies compare favorably with those in observations, and that the shape of the stellar component is misaligned with the dark matter component, with average misalignment angles ranging from $\sim 10^\circ$ to $30^\circ$. In Tenneti et al. (2015), we extended this study to two-point statistics and explored their dependence with mass, luminosity and distance. We found that the intrinsic alignments of massive galaxies in the simulation have a scaling with transverse distance that is consistent with results from observational measurements. Large volume hydrodynamic simulations are proving to be extremely useful in quantifying intrinsic alignment signals. However, they are also very computationally expensive. Hence, it would be useful to develop methods to paint the intrinsic alignments of galaxies onto $N$-body simulations. It is known that the halo shapes and orientations in $N$-body simulations overestimate the intrinsic alignments when compared with observational results (Heymans et al. 2006). Hence, a direct comparison of intrinsic alignments in hydrodynamic and $N$-body simulations is necessary. In this paper, we use the MassiveBlack-II dark matter-only (DMO) simulation that has been performed with the same resolution, box size, initial conditions, and cosmological parameters as the hydrodynamic simulation (MBII) to compare the intrinsic alignments of galaxies in MBII and halos in DMO.

To predict the intrinsic alignment of galaxies from dark matter-only simulations accurately, it is important to have an average mapping that statistically determines the ellipticity and orientation of the stellar matter component of the subhalo with respect to that of the dark matter component. Here, the radius at which the shape of the dark matter subhalo is measured matters, as it has been shown using $N$-body simulations that the shapes of dark matter component change with radius (Allgood et al. 2006; Kuhlen, Diemand & Madau 2007; Schneider, Frenk & Cole 2012). Further, it is also known that the dark matter halo shapes in hydrodynamic simulations are different from those in $N$-body simulations due to the effects of baryonic physics, which leads to rounder shapes (Kazantzidis et al. 2004; Bryan et al. 2013). Here, we study the radial dependence of the distribution of dark matter halo axis ratios in the MBII and DMO simulations, and compare with the shape of the stellar matter component in MBII. We also study the orientation of the stellar shape with the shape of dark matter component in MBII and DMO measured at different radii. The change in the orientation of the dark matter shapes in the subhalos measured at different radii has been previously studied using $N$-body simulations (e.g., Bailin & Steinmetz 2005; Schneider, Frenk & Cole 2012). Using small volume hydrodynamic simulations, Bailin et al. (2005), Deason et al. (2011) and others (see references in the review by Kiessling et al. 2015) found that the inner shape of the dark matter component is well aligned with the galaxy orientation. However, it will be useful to compare the orientation of stellar shape in the hydrodynamic simulation with the shape of the dark matter component measured at different radii in the matched subhalo of a dark matter-only simulation. This comparison is what will enable the mapping of intrinsic alignments in hydrodynamic simulations onto dark matter-only simulations.

This paper is organized as follows. In Section 2, we describe the details of the simulations used in this study followed by the method adopted to determine the shapes of galaxies and the definitions of two-point statistics. In Section 3, we match the subhalos in both simulations and compare shapes and misalignment angles. A brief discussion of the comparison of mass functions and dark matter power spectrum in the two simulations is also included here. In Section 4, we analyze the radial dependence of shapes and orientations of the dark matter component in subhalos. In Section 5, we compare the two-point correlation functions using shapes defined by the dark matter component in MBII and DMO, and the stellar shapes from MBII. Finally, we summarize our conclusions in Section 6.

## 2 METHODS

### 2.1 Simulations

In this study, we use the MassiveBlack-II hydrodynamic (MBII) and Dark Matter Only (DMO) Khandai et al. (2014) simulations. MassiveBlack-II is a state-of-the-art high resolution, large volume, cosmological simulation of structure formation. These simulations have been performed in a cubic periodic box of size $100h^{-1}$Mpc on a side using P-GADGET, which is a hybrid version of the parallel code, GADGET2 (Springel, Di Matteo & Hernquist 2005) that has been upgraded to run on Petaflop-scale supercomputers. The total number of dark matter particles in both the simulations is

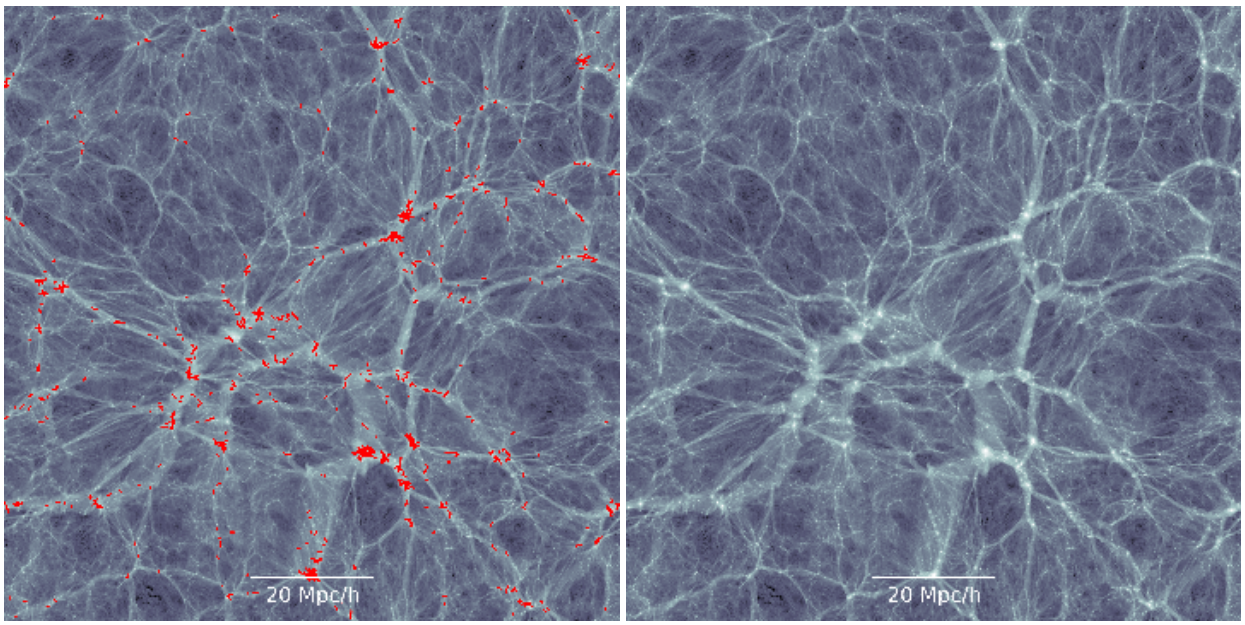


**Figure 1.** Snapshot of the MBII (left) and DMO (right) simulations in a slice of thickness $2h^{-1}$Mpc at $z = 0.06$. The shading represents the density distribution of dark matter, and the red lines show the alignment of stellar shapes in MBII. The length of the lines is proportional to the size of major axis of the ellipse representing stellar shape.

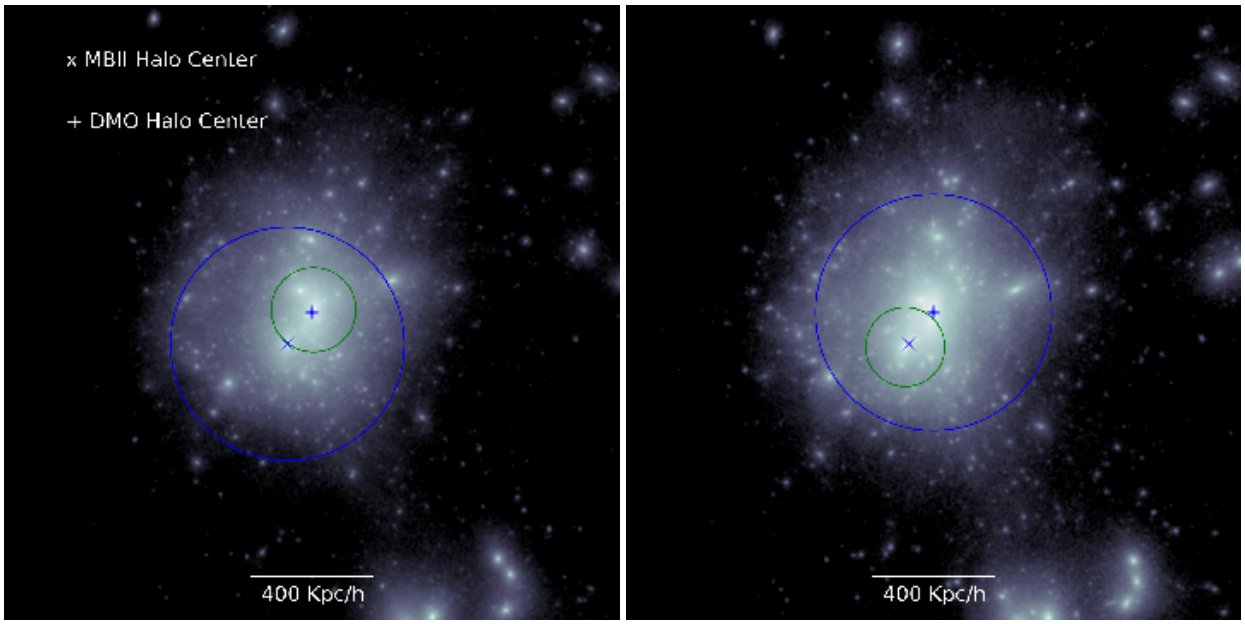


**Figure 2.** Snapshot of a massive halo ($\sim 10^{14}h^{-1}M_{\odot}$) in the MBII (left) and DMO (right) simulations, showing the density distribution of dark matter at $z = 0.06$. The blue and green circles show the virial radii of the subhalos centered at the location with highest density. In both the panels, 'x' and '+' indicate the locations of the halo centers in the MBII and DMO simulations, respectively.

$1792^3$ with an equal initial number of gas particles in the hydrodynamic run. The cosmological parameters are chosen according to WMAP7 (Komatsu et al. 2011), with amplitude of matter fluctuations $\sigma_8 = 0.816$, spectral index $n_s = 0.96$, matter density parameter $\Omega_m = 0.275$, cosmological constant density parameter $\Omega_\Lambda = 0.725$, baryon density parameter $\Omega_b = 0.046$ (in MBII), and Hubble parameter $h = 0.702$. Table 1 shows the box size ($L_{box}$), force softening length ($\epsilon$), total number of particles including dark matter and gas ($N_{part}$), mass of dark matter particle ($m_{DM}$) and initial mass of gas particle ($m_{gas}$) for the two simulations. MBII includes the physics of a multiphase interstellar medium (ISM) model with star formation (Springel & Hernquist 2003), black hole accretion and feedback (Springel, Di Matteo & Hernquist 2005; Di Matteo et al. 2012) in addition to gravity and smoothed-particle hydrodynamics (SPH). Radiative cooling and heating processes are included (as in Katz, Weinberg & Hernquist 1996), as is photoheating due to an imposed ioniz-

**Table 1.** Simulation parameters: box size ($L_{box}$), force softening length ($\epsilon$), number of particles ($N_{part}$), mass of dark matter particle ($m_{DM}$) and mass of gas particle ($m_{gas}$)

| Parameters | Hydrodynamic (MBII) | Dark Matter Only (DMO) |
|---|---|---|
| $L_{box}$ ($h^{-1}$Mpc) | 100 | 100 |
| $\epsilon$ ($h^{-1}$kpc) | 1.85 | 1.85 |
| $N_{part}$ | $2 \times 1792^3$ | $1792^3$ |
| $m_{DM}$ ($h^{-1}M_\odot$) | $1.1 \times 10^7$ | $1.32 \times 10^7$ |
| $m_{gas}$($h^{-1}M_\odot$) | $2.2 \times 10^6$ | 0 |

ing UV background. Further details about the MBII simulation can be found in Khandai et al. (2014). The dark matter-only simulation, DMO, is performed with the same volume, resolution, cosmological parameters and initial conditions as in MBII. Figure 1 shows snapshots of the dark matter distribution in a slice of $2h^{-1}$Mpc thickness at $z = 0.06$ in both the MBII and DMO simulations. As expected, the dark matter distributions appear to be nearly identical on large scales. For further comparison, we also show the dark matter distribution in an isolated halo in Figure 2. Here, we can clearly see small differences in the distribution of dark matter within the dark matter halo virial radius which, as we shall see, can lead to changes in the shapes and orientations of the halos and subhalos.

The halo catalogs in the simulations are generated using the friends of friends (FoF) halo finder algorithm (Davis et al. 1985) with a linking length of 0.2 times the mean inter-particle separation. The subhalo catalogs are generated using the SUBFIND code (Springel et al. 2001) on the halo catalogs. Here subhalos are locally overdense, self-bound groups of particles within the halo. Groups of particles are identified as subhalos if they have at least 20 gravitationally bound particles. When performing our analysis, however, we use only subhalos from the hydrodynamic simulation with at least 1000 dark matter and star particles based on the convergence test in Tenneti et al. (2014).

### 2.2 Shapes of dark matter subhalos

In this section, we describe the measurements of dark matter and stellar matter component shapes in subhalos. We model these shapes as ellipsoids in three dimensions using the eigenvalues and eigenvectors of the reduced inertia tensor. The projected shapes are calculated by projecting the halos and subhalos onto the $XY$ plane and modeling the shapes as ellipses. In 3D, the eigenvectors of the inertia tensor are $\hat{e}_a, \hat{e}_b, \hat{e}_c$ with corresponding eigenvalues $\lambda_a, \lambda_b, \lambda_c$, where $\lambda_a > \lambda_b > \lambda_c$. The eigenvectors represent the principal axes of the ellipsoid, with the lengths of the principal axes $(a, b, c)$ given by the square roots of the eigenvalues $(\sqrt{\lambda_a}, \sqrt{\lambda_b}, \sqrt{\lambda_c})$. The 3D axis ratios are defined as

$$q = \frac{b}{a},\ s = \frac{c}{a} \tag{1}$$

In 2D, the eigenvectors are $\hat{e}'_a, \hat{e}'_b$ with corresponding eigenvalues $\lambda'_a, \lambda'_b$, where $\lambda'_a > \lambda'_b$. The lengths of the major and minor axes are $a' = \sqrt{\lambda'_a}$ and $b' = \sqrt{\lambda'_b}$ with axis ratio $q_{2d} = b'/a'$.

The shapes are determined using an iterative method based on the reduced inertia tensor:

$$\widetilde{I}_{ij} = \frac{\sum_n m_n \frac{x_{ni} x_{nj}}{r_n^2}}{\sum_n m_n} \tag{2}$$

where

$$r_n^2 = \sum_i x_{ni}^2 \tag{3}$$

This definition of inertia tensor gives more weight to particles that are closer to the center which is desirable since it eliminates the bias due to loosely bound particles present in the outer regions of the subhalo. In the iterative method, we first determine the axis ratios by the standard definition of the reduced inertia tensor using all the particles of a given type in the subhalo. Keeping the enclosed volume constant (as in Schneider, Frenk & Cole 2012), we rescale the lengths of the principal axes of ellipsoids accordingly. After this rescaling, we determine the shapes again, discarding particles outside the ellipsoidal volume. This process is repeated until convergence is reached. Our convergence criterion is that the fractional change in axis ratios must be below 1%. We considered the impact of using different definitions of the inertia tensor on the distributions of shapes and the intrinsic alignment two-point correlation functions in a previous study (Tenneti et al. 2015).

### 2.3 Misalignment angle

To study the relative orientation between the shapes defined by the dark matter and stellar matter components in subhalos, we compute the probability distributions of misalignment angles as in Tenneti et al. (2014). If $\hat{e}_{da}$ and $\hat{e}_{ga}$ are the major axes of the shapes defined by the dark matter and stellar matter components, respectively, then we can define the misalignment angle by

$$\theta_m = \arccos(|\hat{e}_{da} \cdot \hat{e}_{ga}|). \tag{4}$$

In previous work (Tenneti et al. 2014, 2015), we studied the distribution of misalignment angles between the shapes of the stellar component and dark matter component in the subhalos of MBII. Here, our aim is to study the misalignment angles between the shapes of stellar component in MBII and the dark matter component in the corresponding subhalo of the DMO simulation. Since the simulations have been performed with the same initial conditions, this is a well-defined comparison, and the resulting distributions will be helpful to paint galaxies onto $N$-body simulations by providing the necessary probability distributions from which to draw the galaxy orientation.

### 2.4 Two-point statistics

To quantify the intrinsic alignments of galaxies with the large-scale density field, we use the ellipticity-direction (ED) and the projected shape-density ($w_{\delta+}$) correlation functions. The ED correlation quantifies the position angle alignments of galaxies in 3D, while the projected shape correlation function can be used to compare against observational measurements that include the 2D shape of the galaxy.

The ED correlation function cross-correlates the orientation of the major axes of subhalos with the large-scale

density field. For a subhalo centered at position $\mathbf{x}$ with major axis direction $\hat{e}_a$, let the unit vector in the direction of a tracer of the matter density field at a distance $r$ be $\hat{\mathbf{r}} = \mathbf{r}/r$. Following the notation of Lee et al. (2008), the ED cross-correlation function is given by

$$\omega(r) = \langle \mid \hat{e}_a(\mathbf{x}) \cdot \hat{\mathbf{r}}(\mathbf{x}) \mid^2 \rangle - \frac{1}{3} \tag{5}$$

which is zero for galaxies randomly oriented according to a uniform distribution.

The matter density field can be represented using either the positions of dark matter particles (in which case the correlation function is denoted by the symbol $\omega_\delta$) or the positions of subhalos (in which case it includes a factor of the subhalo bias, and is simply denoted $\omega$). Here, we only use $\omega_\delta$ to eliminate the effect of subhalo bias.

The projected shape correlation functions are computed to directly compare our results from simulations with observations. Here, we follow the notation of Mandelbaum et al. (2006) to define the galaxy-intrinsic shear correlation function, $\hat{\xi}_{g+}(r_p, \Pi)$ and the corresponding projected two-point statistic, $w_{\delta+}$. Here, $r_p$ is the comoving transverse separation of a pair of galaxies in the $XY$ plane and $\Pi$ is their separation along the $Z$ direction.

If $q_{2d} = b'/a'$ is the axis ratio of the projected shape of the dark matter or stellar matter component of a subhalo, and $\phi$ is the major axis position angle with respect to the reference direction (tracer of the density field), the components of the ellipticity are given by

$$(e_+, e_\times) = \frac{1 - q_{2d}^2}{1 + q_{2d}^2} \left[\cos(2\phi), \sin(2\phi)\right], \tag{6}$$

where $e_+$ refers to the radial component and $e_\times$ is the component at 45°. The matter-intrinsic shear correlation function cross-correlates the ellipticity of galaxies with the matter density field,

$$\hat{\xi}_{\delta+}(r_p, \Pi) = \frac{S_+D - S_+R}{RR} \tag{7}$$

where $S_+$ represents the "shape sample" which is selected on the basis of a threshold or binning in subhalo mass. The dark matter particles used to trace the density field form a "density sample" denoted by $D$. $S_+D$ is the following sum over all shape sample vs. dark matter particle pairs with separations $r_p$ and $\Pi$:

$$S_+D = \sum_{i \neq j | r_p, \Pi} \frac{e_+(j \mid i)}{2\mathcal{R}}, \tag{8}$$

where $e_+(j|i)$ is the + component of the ellipticity of a galaxy ($j$) from the shear sample relative to the direction of a tracer of density field ($i$) selected from the density sample. Here, $\mathcal{R} = (1 - e_{\rm rms}^2)$ is the shear responsivity that converts from distortion to shear (Bernstein & Jarvis 2002), with $e_{\rm rms}$ being the RMS ellipticity per component of the shape sample. $S_+R$ is defined by a similar equation for the correlation of the data sample with a random density field distribution to remove observational systematics in the shear estimates, so we neglect this term here. The $RR$ term in Eq. 7 is given by the expected number of randomly-distributed points in a particular $(r_p, \Pi)$ bin around galaxies in the shape sample.

The projected shape correlation function, $w_{\delta+}(r_p)$ is now given by

$$w_{\delta+}(r_p) = \int_{-\Pi_{\rm max}}^{+\Pi_{\rm max}} \hat{\xi}_{\delta+}(r_p, \Pi)\, {\rm d}\Pi \tag{9}$$

We calculated the correlation functions over the whole length of the box ($100h^{-1}$Mpc) with $\Pi_{\rm max} = 50h^{-1}$Mpc. The projected correlation functions are obtained via direct summation.

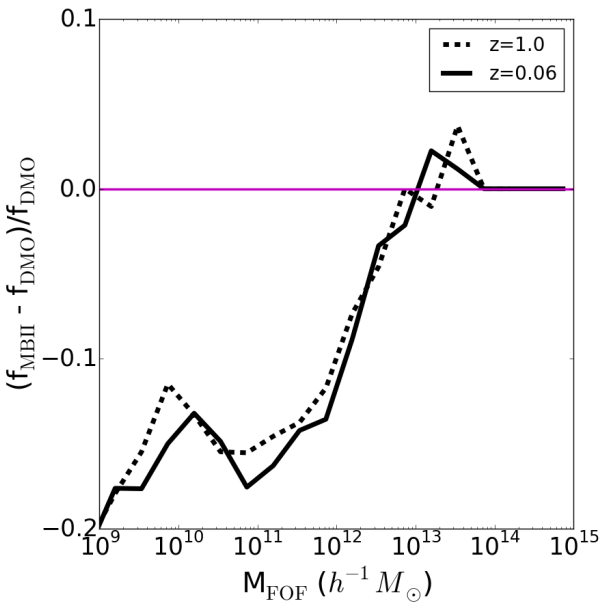


**Figure 3.** Comparison of the halo mass function in MBII and DMO simulations at $z = 1.0$ and $z = 0.06$.

## 3 RESULTS

### 3.1 Mass function

In Figure 3, we compare the mass function of halos in MBII and DMO simulations at redshifts $z = 1$ and $z = 0.06$. At both redshifts, there are differences in the dark matter halo mass function in MBII. There are $\sim 10-20\%$ more halos in the DMO simulation at low masses ($10^9 - 10^{12}h^{-1}M_\odot$). This fraction decreases at higher masses. Velliscig et al. (2014) found similar results using the OWLS simulation with resolved halos in the mass range $10^{12} - 10^{15}h^{-1}M_\odot$ (based on $M_{200}^{\rm mean}$). However, Velliscig et al. (2014) find an even larger suppression in their halo mass function, possibly due to a stronger AGN feedback model. This suppression of mass function can be explained by the decrease in the FOF mass of halos in MBII. To illustrate further, we plotted the median of the fractional difference in the FOF mass of the matched halos of MBII and DMO simulation in Figure 4. We find that the halo mass is smaller in the hydrodynamic simulation by $\sim 10 - 20\%$ in the low mass range.

### 3.2 Matter correlation function and power spectrum

Figure 5 shows a comparison of the 3D dark matter two-point correlation function and power spectrum at $z = 1.0$

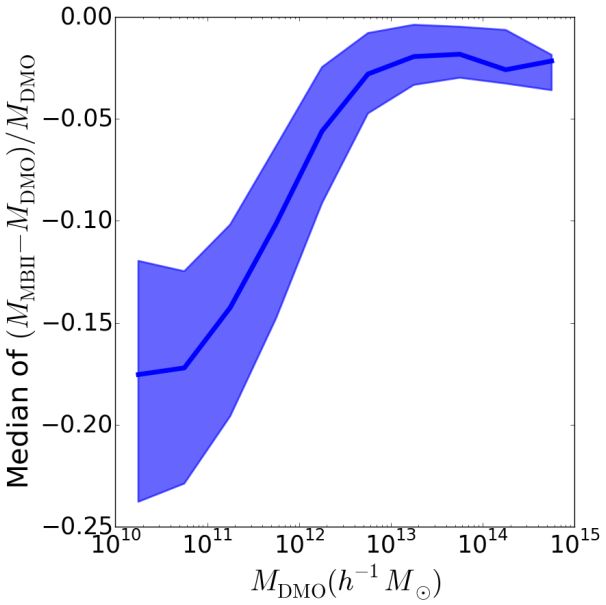


**Figure 4.** Median and scatter (defined using the $16^{\rm th}$ and $84^{\rm th}$ percentiles) of the fractional difference in the FOF mass of matched halos of MBII and DMO simulations at $z = 0.06$.

and $z = 0.06$ in the MBII and DMO simulations. To calculate the two-point correlation function, we randomly subsampled $4 \times 10^5$ dark matter particles and tested that the correlation function has already converged using a smaller subset. The power spectrum is calculated by taking the Fourier transform of the two-point correlation function,

$$P(k) = 4\pi \int_0^{\sqrt{3}\Pi_{\rm max}} \xi(r) r^2 \frac{\sin(kr)}{kr}\,{\rm d}r. \qquad (10)$$

From the left panel of the figure, we observe that $\xi(r)$ is larger at small scales ($< 1h^{-1}$Mpc) in the MBII simulation, presumably due to baryonic physics. At these scales, the correlation function is larger in MBII by a factor of $\sim 10\%$, and the discrepancy is larger at lower redshift. At intermediate scales (above $\sim 1h^{-1}$Mpc), we find that the ratio of the correlation functions approaches unity with no significant redshift dependence. The enhancement of the correlation function at small scales is compensated by a decrease in clustering at scales comparable to the box size.

The right panel of Fig. 5 shows a comparison of the matter power spectra, demonstrating that the dark matter power spectrum in the hydrodynamic run is enhanced by $\sim 10\%$ at $k \gtrsim 10h$/Mpc, with the effect again being stronger at low redshift. In contrast to our results, van Daalen et al. (2011) found that the dark matter power spectrum is suppressed at intermediate scales in the OWLS simulation that included AGN feedback. The purple band in this plot indicates the target precision of $\sim 1$ per cent accuracy in predictions of the matter power spectrum on scales of $0.1h$ Mpc$^{-1} < k < 10h$ Mpc$^{-1}$ (Huterer & Takada 2005; Hearin, Zentner & Ma 2012). This level of accuracy in the theoretical predictions is necessary to avoid systematic errors in constraining cosmological parameters. Zentner et al. (2013); Eifler et al. (2014) and Mohammed & Seljak (2014) discuss approaches to mitigate the potentially large differences in the matter two-point correlations and reduce the uncertainty to the necessary level.

### 3.3 Matching subhalos in MBII and DMO

To make a fair comparison between intrinsic alignments of galaxies and halos in the MBII and DMO simulations, we matched the subhalos in both simulations. The subhalos are matched using the unique ID's of the dark matter particles in both the DMO and MBII simulations. For a given subhalo in the MBII simulation with at least 1000 dark matter and star particles, we identify the subhalo in the DMO simulation that has the highest number of dark matter particles with the same IDs as in the MBII subhalo. This subhalo in the DMO simulation is linked to the subhalo in MBII if the fraction of common dark matter particles is greater than 50% of the total number of dark matter particles in the subhalos of each simulation. Figure 6 shows the matched fraction of subhalos as a function of mass. We observe that the fraction of matched subhalos increases with mass and approaches unity. For the rest of this paper, we will only consider subhalos with mass greater than $10^{10.8}h^{-1}M_\odot$, where the matched fraction exceeds 90%.

The decrease in the fraction of matched subhalos at lower masses is due to an increase in the number of satellite subhalos. The fraction of central subhalos matched even in the lower mass bin, $10^{10.8-11.0}h^{-1}M_\odot$, is $\sim 99\%$. As illustrated in Figure 2, there are small but visible differences in the smallest subhalo population in a matched halo of mass $\sim 10^{14}h^{-1}M_\odot$ (for example, some missing or merged subhalos in MBII). We also attempted to match subhalos using only the 50 innermost dark matter particles, and obtained results that were largely consistent with the method discussed earlier. However, for a small fraction of subhalos, this new method would cause us to link subhalos in the two simulations with very different masses. For example, consider the distribution of dark matter in the MBII and DMO simulations in Figure 2. The blue and green circles show the virial radius of the central subhalo and a nearby satellite subhalo respectively. We can clearly see that the center of the satellite subhalo in MBII is closer to the center of the central subhalo in DMO simulation, which leads to a false match using the 50 closest particles. Hence, we use all the dark matter particles in the subhalo to obtain a consistent match. For similar reasons (such as changes in the location of density peaks), it is not possible to consistently match the satellite subhalos in low mass halos, which is the motivation for our adoption of a lower mass limit of $10^{10.8}h^{-1}M_\odot$.

## 4 SHAPES AND MISALIGNMENT ANGLES

In this section, we investigate the change in the shape and orientation of the subhalos with the distance from their center, which is defined as the location of the most bound particle in the subhalo. This measurement is necessary to understand whether the shape of the stellar matter component traces the (inner) shape of the dark matter component. We show the radial dependence of the shape of the dark matter component in both the MBII and DMO simulations, and compare the orientations at various radii against that of the stellar component in MBII.

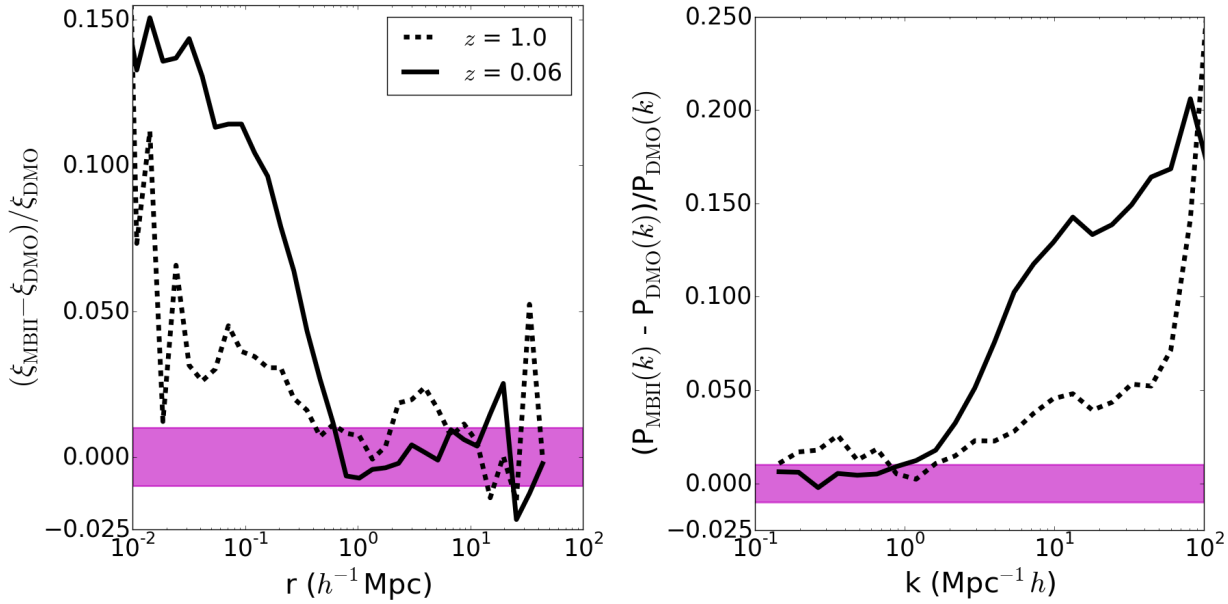


**Figure 5.** Fractional difference between the dark matter two-point correlation functions (left) and power spectra (right) in DMO and MBII simulations at $z = 1.0$ and $z = 0.06$. The shaded regions represent a deviation within $\pm 1\%$.

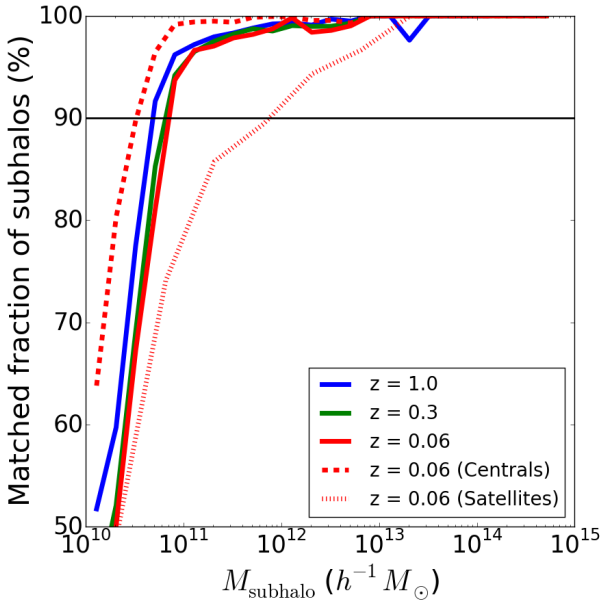


**Figure 6.** Fraction of subhalos matched at $z = 1.0$, 0.3, and 0.06 as a function of the total subhalo mass in the MBII simulation.

### 4.1 Radial dependence of shapes

To calculate the shape of the dark matter component in the subhalo within a given radius, we start with all dark matter particles inside the spherical volume at a given distance from the center and compute the shape using the iterative reduced inertia tensor (Eq. 2). By using the reduced inertia tensor for shape calculation, we still provide more weight to the particles in the inner region of the subhalo, so our resulting shapes should be considered as shapes within a radius rather than at that radius. Hence, the effect of baryonic physics on the dark matter halo shapes in MBII will be evident even for shapes measured out to large radii. For the analysis of shapes, we only consider subhalos with at least 500 particles remaining after the last iteration, excluding fewer than 1% of galaxies. We will compare the distribution of shapes and alignments of the dark matter component calculated within a radial distance of $0.2R_{200}$, $0.6R_{200}$ and $1.0R_{200}$. Here $R_{200}$ is the radius within which the spherically-calculated average density of matter is equal to 200 times the critical density.

The radial dependence of dark matter halo shapes has previously been studied using $N$-body simulations (e.g., Allgood et al. 2006; Schneider, Frenk & Cole 2012) and small-volume hydrodynamic simulations (e.g., Kazantzidis et al. 2004; Abadi et al. 2010; Deason et al. 2011). As in our work, the method used to measure the shapes in Allgood et al. (2006), Deason et al. (2011), and Schneider, Frenk & Cole (2012) is based on the iterative reduced inertia tensor. However, (Kazantzidis et al. 2004) measure shapes using only particles within different radial bins with the reduced inertia tensor, and Abadi et al. (2010) fit ellipsoids to the positions of dark matter particles along the isopotential contours at different radii. Hence, the comparison with some of these previous studies is only qualitative.

In Figure 7, we show the normalized histograms of the dark matter subhalo axis ratios in MBII and DMO calculated with different maximum radii, as well as the axis ratios of the total stellar matter component of MBII. Throughout this section, we use three mass bins: $10^{10.8-11.5}h^{-1}M_\odot$, $10^{11.5-13.0}h^{-1}M_\odot$ and $> 10^{13}h^{-1}M_\odot$ (M1, M2, and M3). Comparing the dark matter subhalo axis ratio distributions in MBII and DMO simulations, we observe that for a given maximum radius, the shapes measured in the hydrodynamic run are more spherical. This finding is in agreement with results from previous studies using smaller-volume hydrodynamic simulations (Kazantzidis et al. 2004; Abadi et al. 2010; Deason et al. 2011). We also find that the axis ratios increase as we go to larger radii, which means that the shape

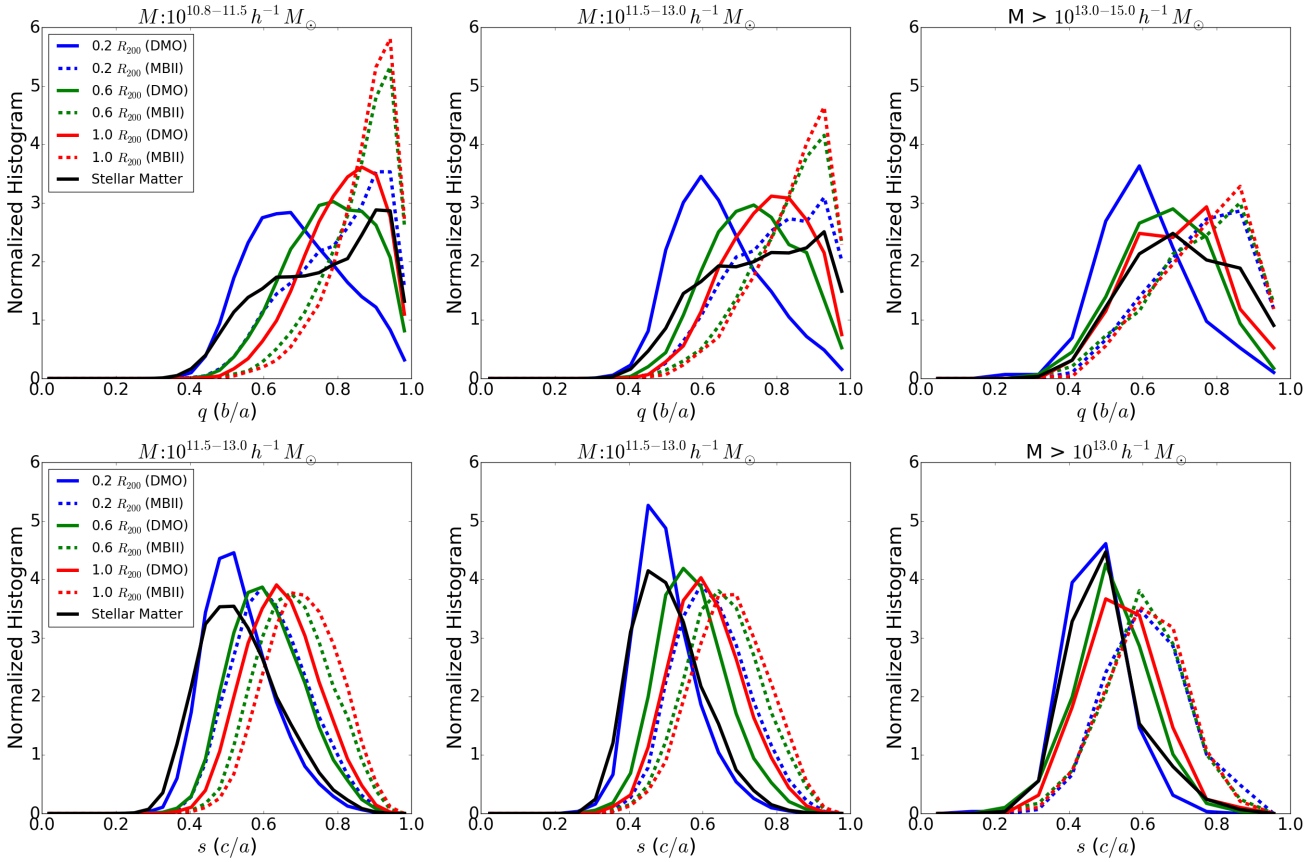


**Figure 7.** Normalized histograms of 3D axis ratios of the dark matter component in matched subhalos in the DMO and MBII simulations, with the shapes measured at different radii ($0.2R_{200}$, $0.6R_{200}$ and $1.0R_{200}$) and also the stellar matter component in MBII. The columns indicate different mass bins, while the top and bottom rows are for $q$ $(b/a)$ and $s$ $(c/a)$, respectively.

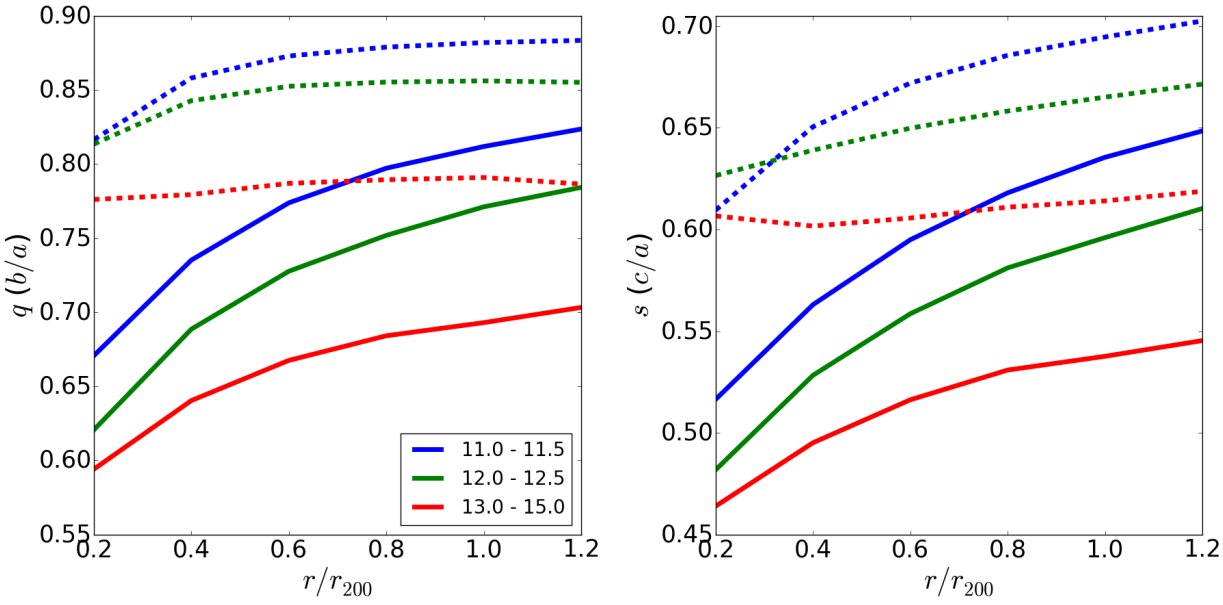


**Figure 8.** Median of the dark matter subhalo axis ratios (left: $q$, right: $s$) in the MBII (dashed lines) and DMO (solid lines) simulations in different mass bins, plotted against the distance to which the shape is measured, at $z = 0.06$.

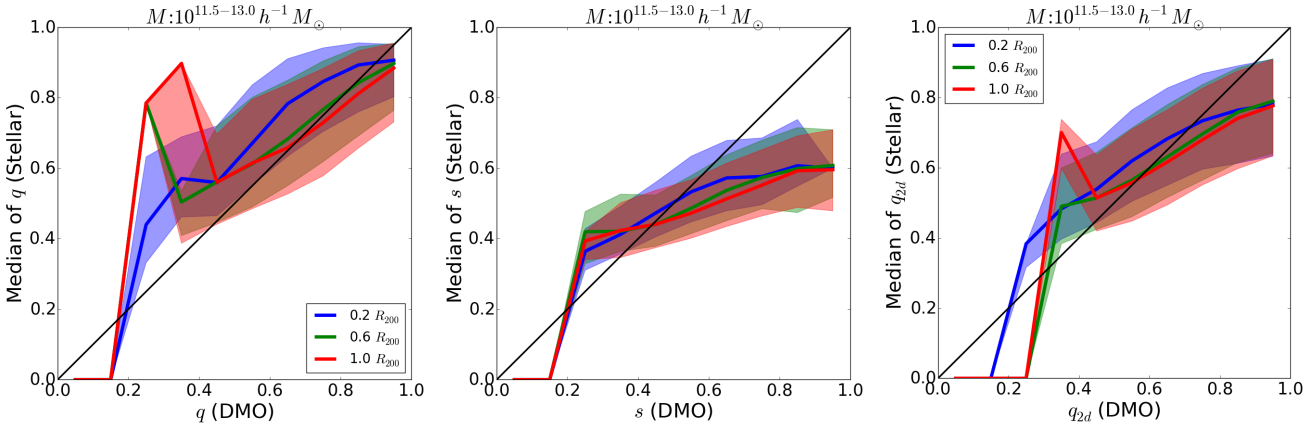


**Figure 9.** Median and scatter (defined using the $16^{\rm th}$ and $84^{\rm th}$ percentiles) in the distribution of the axis ratios (3D and 2D) of the stellar matter component in MBII plotted against the axis ratio of the shape of matched subhalo in the DMO simulation, with the shape measured within different radii ($0.2R_{200}$, $0.6R_{200}$ and $1.0R_{200}$). *Left:* $q$ (3D); *middle:* $s$ (3D); *right:* $q_{2d}$ (2D).

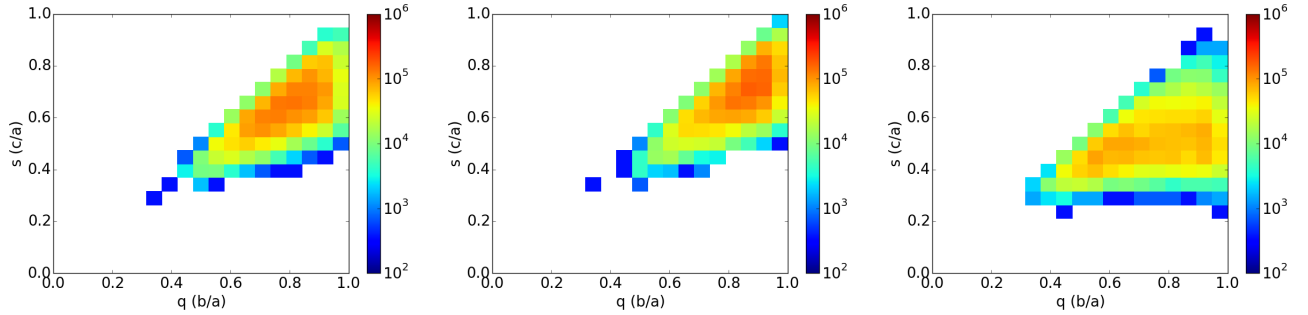


**Figure 10.** Contour plots of 3D axis ratios of the dark matter component in matched subhalos in the DMO (left) and MBII (middle) simulations, and the stellar matter component in MBII (right), in the mass bin M2 at $z = 0.06$.

of the dark matter component is more flattened in the inner regions of the subhalo, again in agreement with previous findings (Deason et al. 2011; Schneider, Frenk & Cole 2012).

To illustrate this effect further, we plot the median axis ratios against the radius within which the shape is measured in Figure 8, in more narrowly-defined mass bins. From the plot, we can see that for a given mass bin, the median axis ratios are higher in MBII. The median values of $q$ and $s$ can be compared against those from Schneider, Frenk & Cole (2012), and qualitatively we reproduce their trend that they decrease at small distances from the subhalo center and at increasing mass. However, this increase in axis ratios is smaller in MB-II than in the DMO simulation. Also, at higher masses, the increase in the median axis ratio with radius is milder than at lower masses. Using smaller-volume hydrodynamical simulations, Abadi et al. (2010) found that the halo axis ratios are independent of radius, and Deason et al. (2011) found that the shapes of dark matter halos are slightly more oblate in the inner regions. These differences are most likely due to the absence of stellar and AGN feedback in those studies, unlike in MBII.

From Figure 7, we see that the axis ratio histograms for the dark matter subhalos in the DMO simulation do not follow those for the galaxy stellar components in MBII, at any radius. This result can be seen more clearly in Figure 9, where we plot the median and scatter in the stellar matter axis ratio distributions in MBII as a function of the DMO dark matter $q$ or $s$ value, for different radii. We see that the scatter in the distribution of axis ratios is large for all radii, so there is no advantage in using the inner shape of the dark matter subhalo in dark matter-only simulations to predict the shape of the stellar component in MBII. For this reason, we only consider the dark matter subhalo axis ratios using all particles in our analysis of two-point statistics.

In Figure 10, we show the contour plot of $q$ versus $s$ for the dark matter shape in DMO and MBII and stellar shape in MBII in the mass bin M2 ($10^{11.5-13.0}h^{-1}M_\odot$). The contour plots indicate that the galaxy shapes are more prolate compared to the shapes of the dark matter component in MBII. We can use the triaxiality parameter, $T = \frac{1-q^2}{1-s^2}$ (Franx, Illingworth & de Zeeuw 1991), to quantify the prolateness or oblateness of the shape. Large (small) values of $T$ imply that the shape is more prolate (oblate). In the mass bin M2, the mean triaxiality of the stellar component shapes is $0.562 \pm 0.003$, while for dark matter shapes in MBII, the mean triaxiality is $0.538 \pm 0.002$. The triaxialities are larger for the dark matter shapes in the DMO simulation with a mean value of $0.600 \pm 0.002$, meaning that the dark matter shapes are more oblate (prolate) in hydrodynamic (dark matter-only) simulations. This conclusion is consistent with results from previous comparisons performed using simulations of smaller volume (Berentzen & Shlosman

2006; Gustafsson, Fairbairn & Sommer-Larsen 2006; Abadi et al. 2010; Deason et al. 2011).

### 4.2 Misalignment angles

In Fig. 11, we show the normalized histograms of the misalignment angles (Eq. 4) between the 3D shape defined by the stellar component of subhalos in MBII and the shape defined by the dark matter component in MBII and DMO (for mass bins M1, M2 and M3). From the plot, we can see that for M3, the alignment of stellar matter in MBII with the dark matter component in DMO (purple curve) is similar to the alignment with the dark matter component in MBII (dashed black curve). This result implies that the shapes of dark matter components in the matched subhalos of MBII and DMO have similar orientations at high mass, which is also shown directly by the green line. Fig. 12 shows a similar result using the projected shapes, with slightly smaller misalignment angles. However, for M1 and M2, it is clear that the stellar matter in MBII is better aligned with the MBII dark matter subhalo than with the corresponding subhalo in DMO.

To check for a connection between galaxy shapes and misalignment angles, we consider the triaxiality parameter, $T$. In Figure 13, we plot the mean misalignment angles between the shapes of stellar matter in MBII with the dark matter shapes in DMO and MBII simulations as a function of triaxiality. From the figure, we can see that as $T$ increases for the stellar shapes and dark matter shapes in MBII, the mean misalignment angles decrease. This means that for stellar and dark matter shapes in MBII which are more prolate, the alignment between the shapes of stellar and the dark matter components is stronger than for those with more oblate shapes. Similarly, for the more prolate dark matter shapes in the DMO simulation, the alignment with the stellar component in MBII is closer. However, the mean misalignment angles decreases by only $\sim 27\%$ while going from $T < 0.33$ to $T > 0.66$ in DMO, which is less than the decrease of $\sim 45\%$ for stellar shapes in MBII. When using galaxy shapes, it is tempting to interpret more oblate shapes as relating to disk galaxies, and thus inferring that disk galaxy shapes are more misaligned with their host dark matter halos than elliptical galaxies. However, we defer a more detailed comparison of the morphologies of galaxies and the connection to misalignment angle distributions in future work.

### 4.3 Radial dependence of misalignment angles

Next, we investigate radial trends in the orientation of the shape of the stellar component in MBII with respect to the dark matter component at different radii in MBII and DMO. Histograms of the misalignment angles when defining the dark matter halo shape within various radii are shown in Figure 14. For comparison, we also show the prediction for a purely random distribution of misalignment angles in 3D. From the plots, we see that in the MBII simulation, the alignment of the stellar component with the dark matter subhalo shape increases as we limit ourselves to smaller radii within the dark matter subhalo. This is expected, as the stellar matter is coupled to the distribution and shape of the dark matter in the inner regions of the subhalo. However, there is no corresponding trend in the DMO simulation, where the misalignment angle distributions have very little dependence on the maximum radius.

From this plot, we can conclude that it is not advantageous to use the inner shape of the dark matter subhalo in a dark matter-only simulation when trying to define mock galaxy shapes and alignments. Since the distribution of misalignment angles with respect to the total dark matter subhalo orientation is not consistent with a uniform random distribution, we can still use these distributions in different mass bins to assign shapes and orientations to galaxies painted onto $N$-body simulations.

## 5 INTRINSIC ALIGNMENT TWO-POINT CORRELATION FUNCTIONS

In this section, we compare the intrinsic alignments in MBII and DMO simulations by analysing the two-point statistics, ellipticity-direction (ED) and the projected density-shape ($w_{\delta+}$) correlation functions defined in Section 2.4. In Figure 15, we compare the ED correlation for the shapes of the dark matter subhalo and stellar matter component in MBII with that for the dark matter subhalos in the DMO simulation, mass bins M1 ($10^{10.8-11.5}h^{-1}M_{\odot}$), M2 ($10^{11.5-13.0}h^{-1}M_{\odot}$), and M3 ($> 10^{13.0}h^{-1}M_{\odot}$). The ED correlation function for the dark matter subhalos in MBII is comparable to that in the DMO simulation on large scales. However, on small scales, we observe a tens of percent decrease in the ED correlation function for the MBII simulation. This finding is possibly due to the dark matter subhalos in MBII being rounder than in DMO, which implies that the dark matter particles assume a distribution within the halos that is closer to spherical, reducing the ED correlation function at smaller scales.

The ED correlation computed using the shape of the stellar matter component in MBII is smaller than that of the dark matter component in DMO (by tens of percent, on all scales). This result is due to the misalignment of the stellar shape with the dark matter subhalo shapes that are determined by the density field. This ratio is relatively scale-independent in the higher mass bins M2 and M3, unlike the ratio of ED for the dark matter subhalos in MBII vs. in DMO. On $0.5 - 5h^{-1}$Mpc scales, the fractional difference of this ratio is on average $\sim 72\%$, 53% and 29% in the mass bins M1, M2, and M3, respectively.

In Fig. 16, we compare the projected shape-density correlation function, $w_{\delta+}$, for the dark matter and stellar matter shapes in MBII with that of the dark matter shape in DMO. Here, $w_{\delta+}$ for the dark matter shape in DMO is higher than the other correlations at all values of $r_p$ and for all mass bins. This finding is expected when comparing the DMO and MBII dark matter subhalos, since the alignment of the dark matter shape with the density field is similar in both simulations, but the dark matter subhalos in MBII are rounder, reducing $w_{\delta+}$ for MBII. If we consider the $w_{\delta+}$ computed using the shapes of the stellar matter components, we observe that at small scales, it is close to the $w_{\delta+}$ of the dark matter shapes in the DMO simulation. This similarity derives from the compensation of two competing effects: the stellar shapes are more misaligned with the density field, lowering

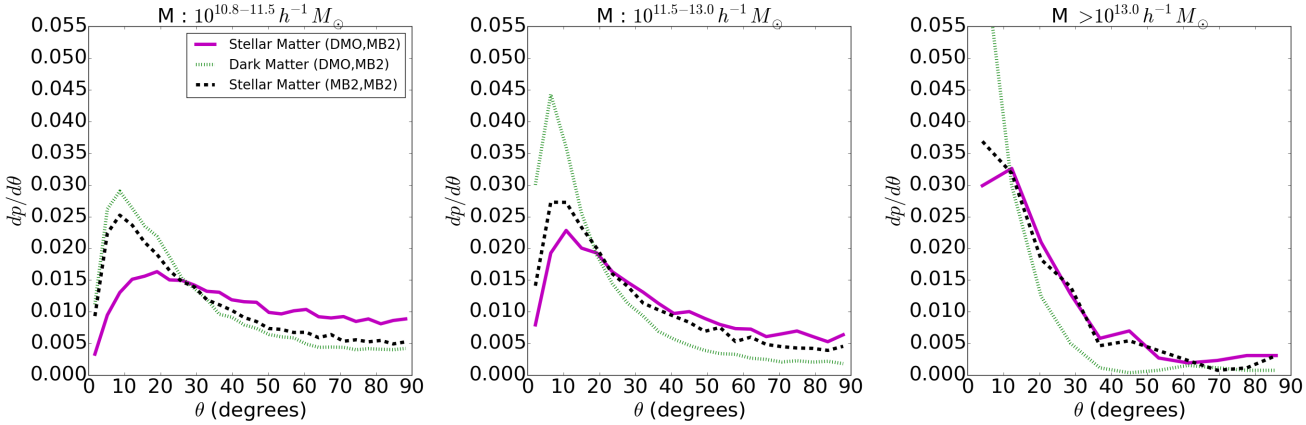


**Figure 11.** Misalignment angle distributions for the 3D shapes of the dark matter component in matched subhalos of DMO and MBII simulations with the stellar matter component in MBII, in mass bins M1, M2 and M3 at $z = 0.06$. Also shown (green line) is the histogram of misalignment angles between the shapes of dark matter subhalos in MBII and DMO.

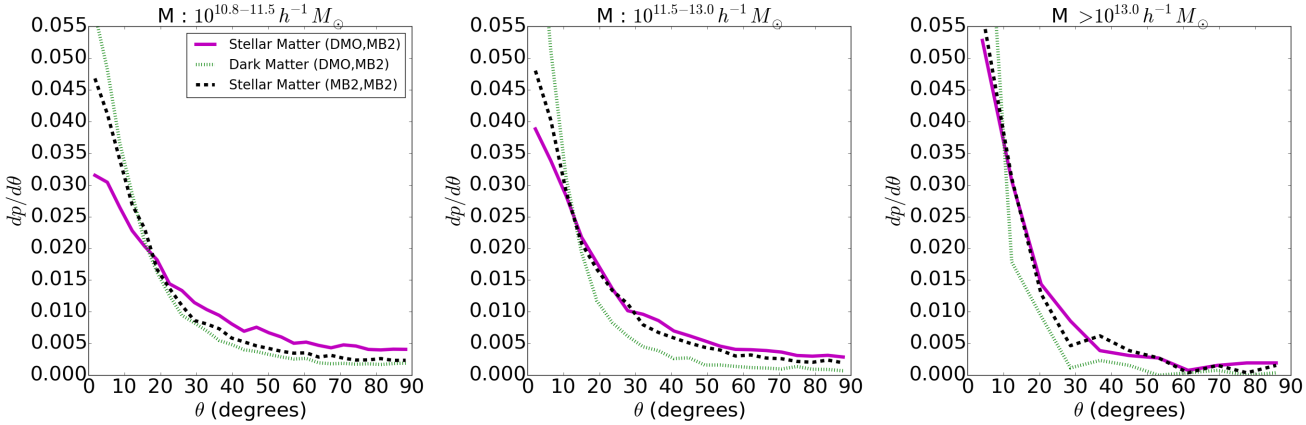


**Figure 12.** Misalignment angle distributions for 2D shapes of the dark matter component in matched subhalos of DMO and MBII with the stellar matter component in MBII, in mass bins M1, M2 and M3 at $z = 0.06$. Also shown (green line) is the histogram of misalignment angles between the shapes of dark matter subhalos in MBII and DMO. This figure is simply the 2D version of Fig. 11.

$w_{\delta+}$, but the stellar shapes have a larger ellipticity, raising $w_{\delta+}$. However, the correlation function computed using stellar component shapes is still $\sim 30-40\%$ smaller than that using DMO subhalos for $0.5 < r_p < 5h^{-1}$Mpc. Due to the limited size of the simulation volume, the uncertainties are large beyond $\sim 5h^{-1}$Mpc. At intermediate scales, we can also see the transition from the 1-halo term to the 2-halo term for the stellar component, whereas for the dark matter component, it is not clearly evident. To illustrate further, we also show the ratio for the 1-halo terms corresponding to $w_{\delta+}$ of the shapes of dark matter and stellar component in MBII. In the lowest mass bin, which has a fairly equal mix of central and satellite subhalos, we observe a change in the shape of the 1-halo term at $\sim 1h^{-1}$Mpc for the stellar component. As the stellar component is more aligned with the inner regions of the dark matter distribution in the subhalo, the 1-halo term drops more significantly in the intermediate scales in comparison to that of the dark matter component.

For a more direct understanding of the effects of alignment versus different shape distributions, we compute a new statistic, $\hat{w}_{\delta+}$, which is defined as the projected shape-density correlation function without ellipticity weighting (i.e., setting $|e| = 1$ for all objects in the shape sample). The results are shown in Figure 17. For the stellar component in MBII, $\hat{w}_{\delta+}$ is smaller than that of the dark matter component in DMO at all scales. For $0.5 < r_p < 5h^{-1}$Mpc, the fractional differences in the correlation function are $\sim 60\%$, 49% and 38% in the mass bins M1, M2, and M3, respectively. Clearly, since the shapes have been normalized to the same value, this must be due only to misalignments between galaxy shapes and the density field. Similarly, the correlation functions for the dark matter subhalo shapes agree on large scales, but that for MBII is smaller than that for DMO on small scales, due to the rounder shapes of the dark matter subhalos (just as was seen for the ED correlation).

## 6 CONCLUSIONS

In this paper, we carried out a comparison of halo and subhalo populations in the MassiveBlack-II (MBII) simulation, and a corresponding dark matter-only simulation (DMO) with the same cosmology, resolution, volume, and initial conditions. First, considering basic halo properties, we com-

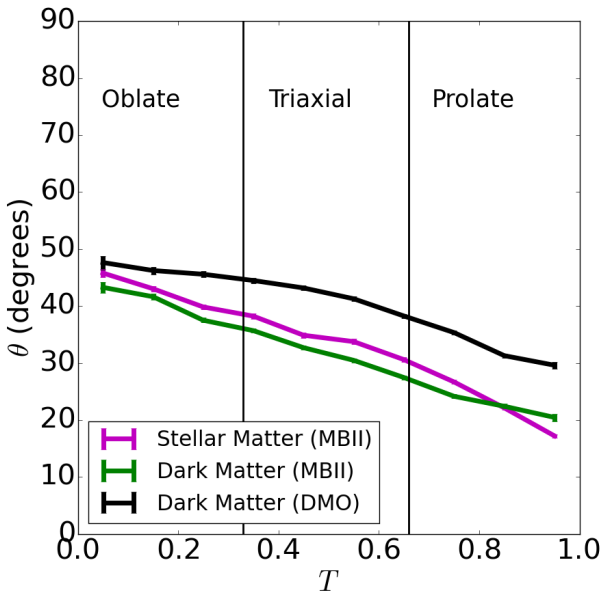


**Figure 13.** Mean of the 3D misalignment angles between the shape of the dark matter component in MBII and DMO with the shape of stellar component in MBII as a function of the triaxiality parameter, $T$ (of the stellar matter component in MBII and the dark matter component in MBII and DMO), in the mass range, $10^{10.8} - 6.0 \times 10^{14} h^{-1} M_\odot$ at $z = 0.06$. The purple line shows the mean misalignment angle between the shape of dark matter component in MBII with the stellar component in MBII plotted against the triaxiality of the shape of stellar component in MBII. Similarly, the green and black lines show the mean misalignment angles between the shapes of dark matter component in MBII and DMO with the stellar component in MBII plotted against the triaxialities of the shapes of dark matter component in MBII and DMO respectively.

pared the halo mass function of the MBII simulation with that of DMO. The mass function is suppressed in the hydrodynamic run by $\sim 10\%$ at $10^{12} h^{-1} M_\odot$, increasing to 20% at $10^{9} h^{-1} M_\odot$. This agrees qualitatively with the findings from the OWLS simulation (Velliscig et al. 2014). The two-point correlation function for the dark matter particles in the two simulations is similar on large scales. On small scales, the two-point correlations are larger for the hydrodynamic run, corresponding to an increased dark matter power spectrum at large $k$ values.

Identifying matching subhalos in the two simulations enables us to directly compare the distribution of axis ratios and shape alignments to understand the effects of baryonic physics. The fraction of matched subhalos decreases as we go to lower masses, but is above 90 per cent for the mass range used in this work. These shapes are also used to calculate and compare the intrinsic alignment two-point statistics.

We measured the shapes of dark matter subhalos in MBII and DMO simulations as a function of radius, by only using particles within a certain distance from the center based on a fixed fraction of the subhalo $R_{200}$. We analyzed the distributions of axis ratios and alignments of shapes measured within $0.2R_{200}$, $0.6R_{200}$, and $1.0R_{200}$. In both simulations, we found that the axis ratios increase with the distance from center, which agrees with previous results in $N$-body simulations (Schneider, Frenk & Cole 2012). We also found that the dark matter subhalo axis ratios in the MBII simulation are higher (rounder) than those in the DMO simulation at all mass ranges due to the effects of baryonic physics, in agreement with previous findings (e.g., Kazantzidis et al. 2004; Abadi et al. 2010; Deason et al. 2011). The galaxy stellar components in MBII have smaller axis ratios than the dark matter subhalos in both simulations, with the fractional difference being larger for the minor-to-major axis ratio, $s$.

The degree of alignment of the stellar component in MBII with the dark matter component in DMO is larger in subhalos of high mass and decreases at lower masses. This trend is qualitatively similar to that of the alignment of the stellar component with the dark matter component in MBII. In subhalos of higher mass, the shapes of the dark matter component in MBII and DMO simulation are well aligned with each other. This alignment is stronger than the alignment of the dark matter shape in MBII with that of stellar component in the same simulation. Comparing the misalignment of the stellar component with shapes of dark matter component measured within different radial distances in MBII, we find that the misalignment angles increase as we go to larger radii within the dark matter subhalo. However, we do not notice a significant change in the misalignment of the stellar component with the shape of dark matter component in DMO measured for different radii. Based on our results from axis ratios and misalignment angles, we concluded that when mapping galaxy alignments from hydrodynamic simulations onto subhalos in dark matter-only simulations, it is not useful to measure the shape of dark matter component at smaller radii in order to trace the shape and orientation of the stellar component. Hence, for the comparison of two-point statistics, we only consider the shapes of dark matter subhalos obtained using all the particles in the subhalo.

Using the shapes of matched subhalos, we compared the intrinsic alignments two-point statistics (ellipticity-direction correlation, or ED, and the projected-shape density correlation, $w_{\delta+}$) of the dark matter and stellar matter in MBII with that of the dark matter component in DMO simulation. The ED correlations of the dark matter component in MBII and DMO agree on large scales. On small scales, the ED correlation function decreases in MBII due to a change in the dark matter profile caused by baryonic physics. For the stellar component, the ED correlation is smaller on all scales due to the misalignment of the stellar component with the dark matter component. This corresponds to a fractional difference ranging from $\sim 30 - 70\%$ for scales around $0.5 - 5 h^{-1}$Mpc, and the decrease is larger in subhalos of lower mass. The $w_{\delta+}$ correlation function for the shapes of dark matter component in MBII are smaller when compared to that of the DMO simulation due to the smaller values of ellipticities, since the shapes are rounder in MBII. For the stellar component, we find that the $w_{\delta+}$ is comparable on large scales and small scales with the $w_{\delta+}$ of the dark matter component in DMO. However, for scales around $0.5 - 5 h^{-1}$Mpc, $w_{\delta+}$ is still smaller for the stellar component by $\sim 30 - 40\%$. At intermediate scales, we find a transition from the 1-halo to 2-halo term that causes a decrease in $w_{\delta+}$ computed using stellar shapes, but this feature is not clearly evident for the $w_{\delta+}$ of the dark matter shape in MBII.

Our results in this paper suggest that the scatter in the distribution of axis ratios of the dark matter subhalo shapes

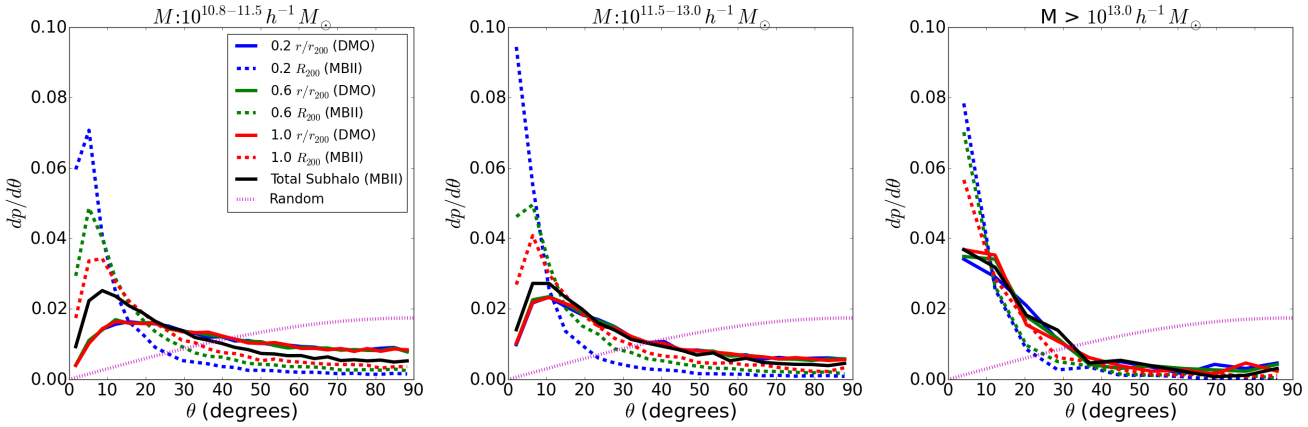


**Figure 14.** Histograms of misalignment angles of 3D shapes of dark matter subhalos in the DMO and MBII simulations (with respect to the shape of the galaxy in MBII) when measuring the subhalo shapes within different radii ($0.2R_{200}$, $0.6R_{200}$, and $1.0R_{200}$) in the mass bins M1 (left), M2 (middle), and M3 (right) at $z = 0.06$.

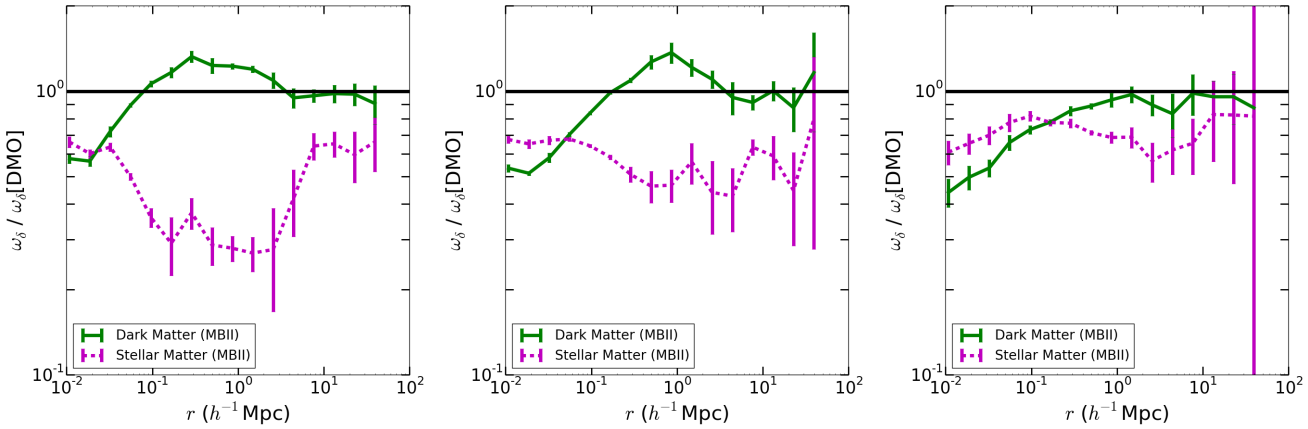


**Figure 15.** Comparison of the ED correlation function, $\omega_\delta(r)$, for the dark matter subhalo and stellar matter components in MBII with respect to that for dark matter subhalos in the DMO simulation, computed separately for M1 (left), M2 (midddle), and M3 (right).

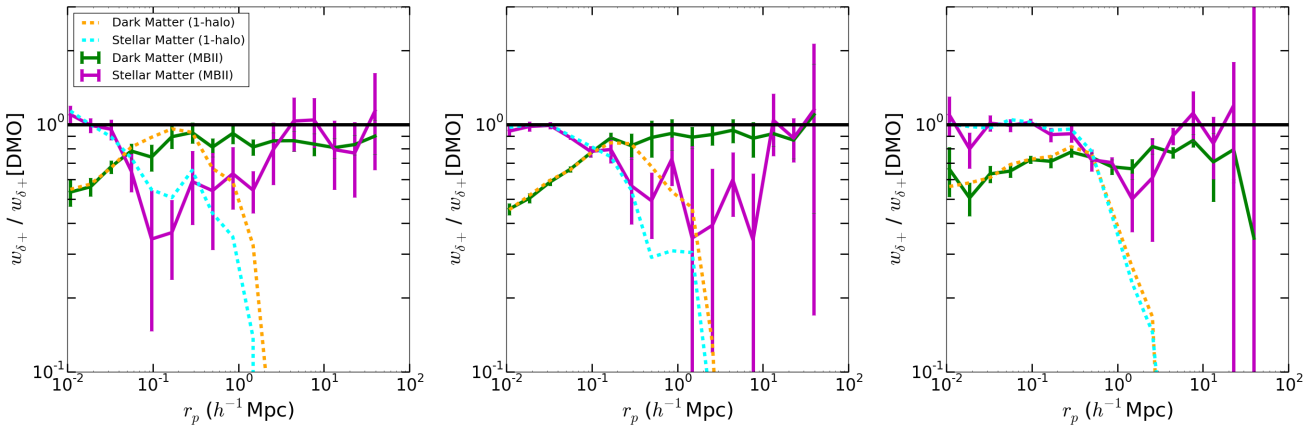


**Figure 16.** Comparison of the projected density-shape correlation, $w_{\delta+}(r_p)$, for the dark matter subhalo and stellar matter components in MBII with respect to that for dark matter subhalos in the DMO simulation, computed separately for M1 (left), M2 (midddle), and M3 (right).

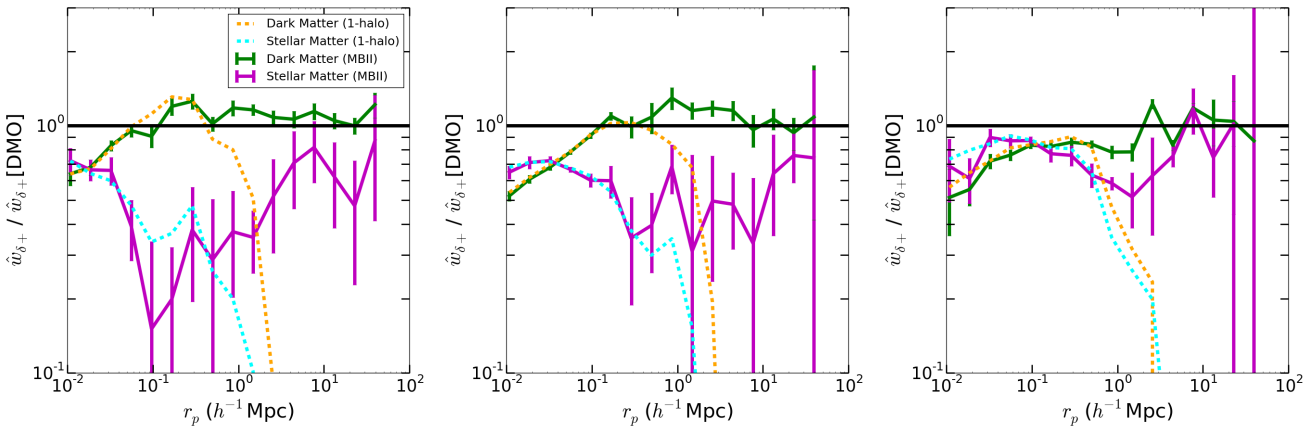


**Figure 17.** Comparison of $\hat{w}_{\delta+}(r_p)$ (projected shape-density correlation function without ellipticity weighting), for the dark matter subhalo and stellar matter components in MBII with respect to that for dark matter subhalos in the DMO simulation, computed separately for M1 (left), M2 (midddle), and M3 (right).

in the DMO simulation is large compared to that of the stellar component in MBII, with significant misalignment in the orientation of shapes. However, the alignments between the galaxies in MBII and the corresponding matched subhalos in the DMO simulation are still significant compared to a uniform random distribution. In future work, we will use these measurements to map the intrinsic alignments of the stellar matter component in hydrodynamic simulations onto dark-matter-only simulations. This is an important step in producing $N$-body based mock catalogs that have realistically-complicated intrinsic alignments for tests of weak lensing analysis methods in future surveys.

## ACKNOWLEDGMENTS

AT and RM acknowledge the support of NASA ROSES 12-EUCLID12-0004. We thank Rachel Bean, Jonathan Blazek, Nick Gnedin, Katrin Heitmann, Michael Schneider and other member of the LSST-DESC collaboration for providing helpful feedback on this work. TDM has been funded by the National Science Foundation (NSF) PetaApps, OCI-0749212 and by NSF AST-1009781 and ACI-1036211. AK was supported in part by JPL, run under a contract by Caltech for NASA. AK was also supported in part by NASA ROSES 13-ATP13-0019. This research used resources of the National Energy Research Scientific Computing Center (NERSC), a DOE Office of Science User Facility supported by the Office of Science of the U.S. Department of Energy under Contract No. DE-AC02-05CH11231.

## REFERENCES

Abadi M. G., Navarro J. F., Fardal M., Babul A., Steinmetz M., 2010, MNRAS, 407, 435
Albrecht A. et al., 2006, arXiv, arXiv:astro-ph/0609591
Allgood B., Flores R. A., Primack J. R., Kravtsov A. V., Wechsler R. H., Faltenbacher A., Bullock J. S., 2006, MNRAS, 367, 1781
Bailin J. et al., 2005, ApJ, 627, L17
Bailin J., Steinmetz M., 2005, ApJ, 627, 647
Berentzen I., Shlosman I., 2006, ApJ, 648, 807
Bernstein G. M., Jarvis M., 2002, AJ, 123, 583
Blazek J., Vlah Z., Seljak U., 2015, arXiv, arXiv:150402510B
Bridle S., King L., 2007, New Journal of Physics, 9, 444
Bryan S. E., Kay S. T., Duffy A. R., Schaye J., Dalla Vecchia C., Booth C. M., 2013, MNRAS, 429, 3316
Catelan P., Kamionkowski M., Blandford R. D., 2001, MNRAS, 320, L7
Croft R. A. C., Metzler C. A., 2000, ApJ, 545, 561
Davis M., Efstathiou G., Frenk C. S., White S. D. M., 1985, ApJ, 292, 371
Deason A. J. et al., 2011, MNRAS, 415, 2607
Di Matteo T., Khandai N., DeGraf C., Feng Y., Croft R. A. C., Lopez J., Springel V., 2012, ApJ, 745, L29
Dubois Y. et al., 2014, MNRAS, 444, 1453
Eifler T., Krause E., Dodelson S., Zentner A., Hearin A., Gnedin N., 2014, arXiv, arXiv:1405.7423E
Franx M., Illingworth G., de Zeeuw T., 1991, ApJ, 383, 112
Gustafsson M., Fairbairn M., Sommer-Larsen J., 2006, Phys.Rev.D, 74, 123522
Hearin A. P., Zentner A. R., Ma Z., 2012, JCAP, 4, 34
Heavens A., Refregier A., Heymans C., 2000, MNRAS, 319, 649
Heymans C., White M., Heavens A., Vale C., van Waerbeke L., 2006, MNRAS, 371, 750
Hirata C. M., Seljak U., 2004, Phys.Rev.D, 70, 063526
Huterer D., Takada M., 2005, Astroparticle Physics, 23, 369
Jing Y. P., 2002, MNRAS, 335, L89
Joachimi B. et al., 2015, arXiv, arXiv:150405456J
Joachimi B., Semboloni E., Hilbert S., Bett P. E., Hartlap J., Hoekstra H., Schneider P., 2013, MNRAS, 436, 819
Katz N., Weinberg D. H., Hernquist L., 1996, ApJS, 105, 19
Kazantzidis S., Kravtsov A. V., Zentner A. R., Allgood B., Nagai D., Moore B., 2004, ApJ, 611, L73
Khandai N., Di Matteo T., Croft R., Wilkins S. M., Feng Y., Tucker E., DeGraf C., Liu M.-S., 2014, arXiv, arXiv:1402.0888
Kiessling A. et al., 2015, arXiv, arXiv:150405546K
Kirk D. et al., 2015, arXiv, arXiv:150405465K

Komatsu E. et al., 2011, ApJS, 192, 18
Kuhlen M., Diemand J., Madau P., 2007, ApJ, 671, 1135
Laureijs R. et al., 2011, arXiv, arXiv:1110.3193L
Lee J., Springel V., Pen U.-L., Lemson G., 2008, MNRAS, 389, 1266
LSST Science Collaboration et al., 2009, arXiv, arXiv:0912.0201L
Mandelbaum R., Hirata C. M., Ishak M., Seljak U., Brinkmann J., 2006, MNRAS, 367, 611
Mohammed I., Seljak U., 2014, MNRAS, 445, 3382
Schneider M. D., Bridle S., 2010, MNRAS, 402, 2127
Schneider M. D., Frenk C. S., Cole S., 2012, JCAP, 5, 30
Spergel D. et al., 2015, arXiv, arXiv:1503.03757
Springel V., Di Matteo T., Hernquist L., 2005, MNRAS, 361, 776
Springel V., Hernquist L., 2003, MNRAS, 339, 289
Springel V., White S. D. M., Tormen G., Kauffmann G., 2001, MNRAS, 328, 726
Tenneti A., Mandelbaum R., Di Matteo T., Feng Y., Khandai N., 2014, MNRAS, 441, 470
Tenneti A., Singh S., Mandelbaum R., Matteo T. D., Feng Y., Khandai N., 2015, MNRAS, 448, 3522
Troxel M. A., Ishak M., 2014, arXiv, arXiv:1407.6990T
van Daalen M. P., Schaye J., Booth C. M., Dalla Vecchia C., 2011, MNRAS, 415, 3649
Velliscig M. et al., 2015, arXiv, arXiv:150404025V
Velliscig M., van Daalen M. P., Schaye J., McCarthy I. G., Cacciato M., Le Brun A. M. C., Vecchia C. D., 2014, MNRAS, 442, 2641
Weinberg D. H., Mortonson M. J., Eisenstein D. J., Hirata C., Riess A. G., Rozo E., 2013, Phys.Rep., 530, 87
Zentner A. R., Semboloni E., Dodelson S., Eifler T., Krause E., Hearin A. P., 2013, Phys.Rev.D, 87, 043509